

OUGS: Active View Selection via Object-aware Uncertainty Estimation in 3DGS

Haiyi Li¹ Qi Chen¹ Denis Kalkofen¹ Hsiang-Ting Chen^{1†}

Abstract

Recent advances in 3D Gaussian Splatting (3DGS) have achieved state-of-the-art results for novel view synthesis. However, efficiently capturing high-fidelity reconstructions of specific objects within complex scenes remains a significant challenge. A key limitation of existing active reconstruction methods is their reliance on scene-level uncertainty metrics, which are often biased by irrelevant background clutter and lead to inefficient view selection for object-centric tasks. We present OUGS, a novel framework that addresses this challenge with a more principled, physically-grounded uncertainty formulation for 3DGS. Our core innovation is to derive uncertainty directly from the **explicit physical parameters** of the 3D Gaussian primitives (e.g., position, scale, rotation). By propagating the covariance of these parameters through the rendering Jacobian, we establish a highly interpretable uncertainty model. This foundation allows us to then seamlessly integrate semantic segmentation masks to produce a targeted, **object-aware** uncertainty score that effectively disentangles the object from its environment. This allows for a more effective active view selection strategy that prioritizes views critical to improving object fidelity. Experimental evaluations on public datasets demonstrate that our approach significantly improves the efficiency of the 3DGS reconstruction process and achieves higher quality for targeted objects compared to existing state-of-the-art methods, while also serving as a robust uncertainty estimator for the global scene.

CCS Concepts

• **Computing methodologies** → **Image-based rendering**; Object detection; Computational photography;

1. Introduction

Efficient 3D scene reconstruction is a foundational goal in computer vision and robotics. The advent of Neural Radiance Fields (NeRF) [MST*20] marked a breakthrough, enabling photorealistic novel view synthesis by learning implicit volumetric representations. More recently, 3D Gaussian Splatting (3DGS) [KKLD23] has emerged as a compelling alternative. By modeling scenes with explicit 3D Gaussian primitives and leveraging a fast, differentiable rasterization pipeline, 3DGS achieves real-time rendering speeds without compromising visual fidelity, addressing the high computational cost that limits NeRF’s practicality.

Despite these advances, both NeRF and 3DGS remain highly data-intensive, typically requiring dense image captures to produce high-quality reconstructions [NBM*21, CKD*25]. This motivates the need for active reconstruction [CLK11], where a human or robotic agent actively selects a minimal subset of views that maximally reduces uncertainty. Achieving this requires models to estimate their own information needs in real-time—a capability that hinges on accurate uncertainty estimation.

In this context, recent work has explored incorporating uncertainty into both NeRFs [GRS*24, KMKS24] and 3DGS. For the lat-

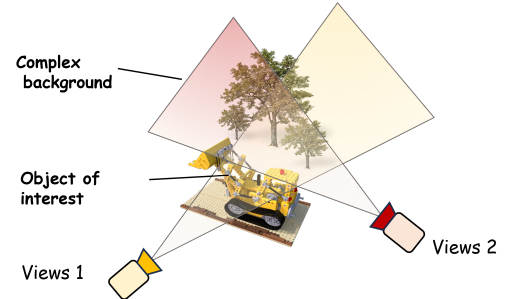


Figure 1: A complex background can inflate image-level uncertainty and mislead active view selection away from the object of interest.

ter, emerging research has introduced methods based on ensemble variance [HD25] or Fisher Information approximations [JLD24]. However, these pioneering methods share a fundamental limitation: they typically estimate uncertainty at the scene level. As illustrated in Figure 1, a global uncertainty score is often dominated by complex but irrelevant background clutter, misleading the view selection process. This is particularly problematic for the growing number of applications where the primary goal is not to reconstruct

[†] Corresponding author: tim.chen@adelaide.edu.au

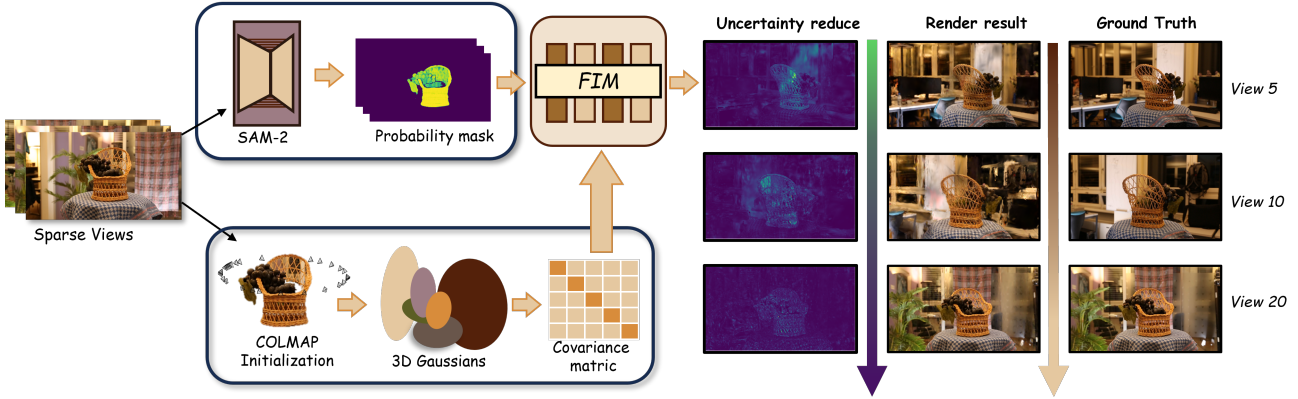


Figure 2: **Object-aware uncertainty guides 3DGS view planning for precise object reconstruction.** Our physically-grounded uncertainty model, derived from the explicit parameters of the 3D Gaussians, is combined with a semantic mask to generate an object-level uncertainty score. This score effectively guides the active view selection to improve object fidelity, as shown for 5, 10, and 20 selected views.

an entire environment, but to capture a **specific object of interest** with the highest possible fidelity.

To address this critical gap, we introduce OUGS, a framework designed specifically for object-centric active reconstruction (Figure 2). Our work is built upon a key insight: to effectively isolate an object’s uncertainty, one must first model uncertainty from a more fundamental, physically-grounded source. Instead of deriving uncertainty from the abstract weights of an implicit neural network, as is common practice, our method is the first to establish a rigorous framework that quantifies uncertainty directly from the **explicit physical parameters** of the 3D Gaussian primitives—their position, scale, rotation, and appearance.

We begin by treating these parameters as random variables and propagate their covariance through the differentiable rendering pipeline via the Jacobian. This yields a pixel-wise visual uncertainty that is not only robust but also highly interpretable. This physically-grounded foundation allows us to then seamlessly integrate semantic masks to disentangle the uncertainty of a target object from its environment. To ensure scalability, we approximate the parameter covariance using a diagonal Fisher Information Matrix (FIM), updated efficiently through an exponential moving average. This complete formulation enables an active view selection strategy that is powerfully and precisely focused on the object of interest. Our comprehensive evaluations demonstrate that this approach facilitates informed next-best-view selection, substantially enhancing both the interpretability and efficiency of the object reconstruction process.

Our contributions are threefold:

- We introduce a novel active reconstruction framework specifically designed for **object-centric tasks** in 3DGS, addressing a key limitation of existing scene-level methods.
- We propose a new, **physically-grounded uncertainty model** based on the explicit parameters of 3D Gaussians, offering greater accuracy and interpretability compared to implicit, weight-based approaches.

- Through extensive experiments, we demonstrate that our method significantly outperforms state-of-the-art approaches in object-focused reconstruction while maintaining strong performance on global scene metrics.

2. Related Work

2.1. Uncertainty in 3D Splatting

Quantifying uncertainty in 3DGS is an emerging research area crucial for real-world applications. Current approaches can be categorized into four main directions: **1) Variational/Bayesian.** A principled approach is to treat Gaussian parameters as distributions. Li & Cheung [LC24] use hierarchical Bayesian priors, while Savant et al. [SVM24] employ variational inference. While mathematically rigorous, these methods incur significant computational overhead (2–3x inference cost), limiting their real-time applicability. **2) Sensitivity Pruning.** Alternatively, some methods measure the model’s sensitivity to its parameters. PUP 3D-GS, for instance, uses a Hessian-based metric to prune Gaussians with high uncertainty. This approach is efficient but offers a less direct measure of predictive uncertainty. **3) Learned Uncertainty Fields.** Another paradigm trains an auxiliary network to directly predict uncertainty. UNG-GS [TCZ*25] adds a Spatial Uncertainty Field for sparse inputs, while Han & Dumery [HD25] learn a view-dependent field. These methods are flexible but risk producing uncalibrated or physically implausible estimates. **4) Information-Theoretic.** Finally, information theory can be used to quantify the information gain of new views. GauSS-MI [XCZ*25], for instance, selects views that maximize mutual information. While powerful for view selection, this paradigm focuses on the information value of potential views rather than the inherent uncertainty of the current reconstruction.

Our work carves a distinct path by adopting an efficient, FIM-based approximation of parameter uncertainty. We apply this formulation directly to the problem of *object-centric active view selection*—a critical application gap not fully addressed by prior works.

2.2. Uncertainty for Active View Selection

Active view selection, or Next-Best-View (NBV) planning, is a long-standing problem in computer vision and robotics [CLK11], aiming to intelligently choose views to maximize reconstruction quality while minimizing cost. Methodologies have evolved significantly over time. **1) Traditional and Geometric Methods.** Early approaches in robotics often relied on geometric heuristics. For instance, receding-horizon planners like the one by Bircher et al. [BKA*16] aim to maximize the exploration of unknown free space using occupancy maps. Other classical NBV methods use voxel-grid representations and select views based on metrics like Shannon entropy or frontier exploration [KSH22]. While effective for coverage, these discretized methods can struggle to capture fine geometric details and are less suited for the continuous representations used in modern neural rendering. **2) Uncertainty in Neural Rendering.** The rise of neural rendering has spurred a new wave of uncertainty-driven NBV methods. For NeRFs, ActiveNeRF [PLSH22] selects views by minimizing rendered color variance, while FisherRF [JLD24] proposes using Fisher information gain as a more principled metric. These ideas have been extended to 3DGS; Pop-GS [WAM*25] also employs a Fisher matrix, and GauSS-MI [XCZ*25] maximizes mutual information. A common thread connects these powerful methods: they compute a global, scene-level score. This design choice leads to a critical limitation: they are agnostic to semantic importance, meaning a complex but irrelevant background can dominate view selection. **3) Other View Selection Paradigms.** Beyond uncertainty and information-theoretic approaches, other paradigms have been explored. Learning-based methods, such as NeurAR [RZH*23], employ reinforcement learning to train an agent that learns an optimal view selection policy directly from simulation. Concurrently, other works focus on explicitly modeling visibility. For instance, Neural Visibility Fields [XDM*24] learn to predict which parts of a scene are visible from a given viewpoint, guiding selection towards views that maximize observable new area. While powerful, these methods either require extensive training or shift the focus from reconstruction fidelity to geometric coverage.

Our work addresses the critical limitation of scene-level uncertainty methods. By introducing an object-aware mechanism, we enable the view selection process to focus on the semantically important regions of the scene, a challenge not explicitly addressed by any of these prior paradigms.

3. Method

3.1. Preliminary: 3D Gaussian Splatting

Our method builds upon the 3D Gaussian Splatting (3DGS) framework [KKLD23], which represents a scene as a collection of anisotropic 3D Gaussian primitives $\mathcal{G} = \{\mathcal{G}_i\}_{i=1}^{N_g}$. To ground our uncertainty analysis, we first provide a detailed list of the parameters used in the differentiable rendering pipeline. Each Gaussian \mathcal{G}_i is fully described by a parameter vector θ_i :

$$\theta_i = \left[\underbrace{\mu_i}_{\text{Center}}, \underbrace{s_i}_{\text{Scale}}, \underbrace{\mathbf{q}_i}_{\text{Rotation}}, \underbrace{\alpha_i}_{\text{Opacity}}, \underbrace{\mathbf{f}_i^{\text{dc}}, \mathbf{f}_i^{\text{sh}}}_{\text{Color (SH)}} \right]^T \quad (1)$$

where the components are:

- **Geometry:** The 3D center $\mu_i \in \mathbb{R}^3$, an anisotropic scaling vector $s_i \in \mathbb{R}_+^3$, and an orientation quaternion $\mathbf{q}_i \in \mathbb{S}^3$. Together, these define the Gaussian’s position, size, and orientation.
- **Appearance:** A scalar opacity value $\alpha_i \in \mathbb{R}$ and view-dependent color modeled by Spherical Harmonics (SH). The color is parameterized by the degree-0 (DC) term $\mathbf{f}_i^{\text{dc}} \in \mathbb{R}^3$ and a set of higher-order coefficients $\mathbf{f}_i^{\text{sh}} \in \mathbb{R}^{3 \times 15}$.

A visual breakdown of these parameters is provided in Figure 3 shows these parameters visually.

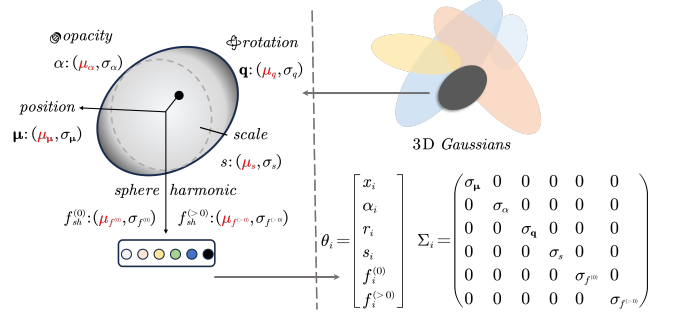


Figure 3: **The parameterization of a 3D Gaussian primitive.** Each Gaussian, the fundamental building block of our scene representation, is defined by a set of explicit physical parameters. Our method’s core innovation lies in directly quantifying the uncertainty of these physical parameters.

Rendering in 3DGS uses a differentiable splatting approach based on standard alpha compositing. First, the 3D Gaussians are projected onto the 2D image plane and sorted in front-to-back order based on their depth. The color $C(u)$ for a pixel u is then accumulated as:

$$C(u) = \sum_{i \in \mathcal{I}(u)} c_i(u) \alpha'_i(u) \prod_{j=1}^{i-1} (1 - \alpha'_j(u)) \quad (2)$$

where $\mathcal{I}(u)$ is the ordered list of Gaussians overlapping the pixel u , $c_i(u)$ is the view-dependent color evaluated from SH. The effective opacity $\alpha'_i(u)$ is determined by modulating the Gaussian’s learned opacity parameter α_i by its projected 2D profile at the pixel location.

3.2. Mapping 3D Gaussian Parameter Uncertainty to Pixel-wise Object-aware Uncertainty

To quantify uncertainty, we treat the parameter vector of each Gaussian as a random variable and initialize it with a Gaussian prior, $\theta_i \sim \mathcal{N}(\theta_i^0, \Sigma_i^0)$. For notational clarity, we stack the per-Gaussian covariances into a block-diagonal matrix

$$\Sigma = \text{diag}(\Sigma_1, \dots, \Sigma_{N_g}) \in \mathbb{R}^{d \times d} \quad (3)$$

where $d = N_g \cdot d_g$. Throughout the rest of this section, Σ refers to this global covariance, while Σ_i denotes its i -th block.

We then project the uncertainty of the 3DGS parameters into pixel space and describe how it interacts with a soft object mask.

Here, we present simplified expressions; full derivations and a second-order error bound are provided in the Appendix.

Decomposition of Uncertainty Sources. A key advantage of our explicit, parameter-centric formulation is the ability to decompose the total uncertainty into its underlying physical sources. We can partition the Gaussian parameter vector θ_i into a **geometry** component, $\theta_i^g = [\mu_i, \mathbf{s}_i, \mathbf{q}_i]^\top$, and an **appearance** component, $\theta_i^a = [\alpha_i, \mathbf{f}_i^{\text{dc}}, \mathbf{f}_i^{\text{sh}}]^\top$. Consequently, the total parameter vector θ and its Jacobian J_u can be similarly partitioned:

$$\theta = \begin{bmatrix} \theta^g \\ \theta^a \end{bmatrix}, \quad J_u = \begin{bmatrix} J_u^g & J_u^a \end{bmatrix} \quad (4)$$

where $J_u^g = \partial C(u)/\partial \theta^g$ and $J_u^a = \partial C(u)/\partial \theta^a$. Assuming independence between geometric and appearance parameters (a reasonable simplification enforced by our diagonal FIM approximation), the pixel-wise color covariance from Eq. 6 can be expressed as a sum of two distinct sources:

$$\Sigma_C(u) \approx \underbrace{J_u^g \Sigma^g (J_u^g)^\top}_{\text{Geometric Uncertainty}} + \underbrace{J_u^a \Sigma^a (J_u^a)^\top}_{\text{Appearance Uncertainty}} \quad (5)$$

This decomposition is theoretically significant. It allows us to differentiate between uncertainty arising from poorly constrained object geometry (e.g., ambiguous boundaries, fine structures) and uncertainty from poorly observed appearance (e.g., complex materials, view-dependent effects). Implicit methods like FisherRF, which operate on abstract network weights, lack this inherent interpretability.

Pixel-wise uncertainty Assume complete set of scene parameters $\theta = \{\theta_i\}$ and θ^* is the MAP estimate after optimization. For small parameter perturbations $\delta\theta = \theta - \theta^*$, the change in pixel color $\delta C(u)$ can be linearly approximated using a first-order Taylor expansion:

$$\delta C(u) \approx J_u \delta\theta$$

where with Jacobian $J_u = \partial C(u; \theta)/\partial \theta \in \mathbb{R}^{3 \times d}$. Given $\mathbb{E}[\delta\theta] = 0$ under a prior normal distribution, the induced pixel-colour covariance can be written as

$$\Sigma_C(u) = \text{Var}[C(u; \theta)] \approx J_u \Sigma J_u^\top \quad (6)$$

where Σ is the full parameter covariance. Eq 6 shows that the Jacobian acts as a lever arm that magnifies (or attenuates) each parameter’s uncertainty in proportion to that parameter’s influence on the pixel [Bon08].

Pixel-wise object-aware uncertainty To estimate the uncertainty of a specific object k , we introduce a soft mask $M_k(u) \in [0, 1]$ based on semantic probabilities. This allows us to define an object-specific pixel covariance $\Sigma_{C,k}(u)$ by masking the standard error propagation formula:

$$\Sigma_{C,k}(u) = (M_k(u))^2 (J_u \Sigma J_u^\top) \quad (7)$$

The mask term $M_k(u)$ is squared because covariance propagates quadratically via the Jacobian and its transpose.

3.3. Updating Uncertainty With FIM

While our formulation provides a physically interpretable model of uncertainty, direct computation of the full covariance matrix Σ is intractable. We therefore approximate it with the inverse of the Fisher Information Matrix (FIM), $\Sigma \simeq \sigma^2 \mathcal{I}^{-1}$ [LMV*17]. Crucially, our FIM is defined over the space of the 3D Gaussians’ physical parameters, capturing how perturbations in geometry and appearance affect the rendered output. This stands in contrast to implicit-representation methods where the FIM is computed over abstract neural network weights.

Diagonal FIM as a Parameter Decoupling Assumption. To ensure computational tractability, we make a key simplifying assumption: we approximate the full FIM with its diagonal entries only, effectively assuming that the different physical parameters of a Gaussian are locally independent. This diagonal approximation, $\mathcal{I} \approx \text{diag}(\mathcal{I})$, aligns perfectly with the uncertainty decomposition presented in Eq. 5. It implies that a Gaussian’s geometric uncertainty (e.g., in its position, μ_i) is decoupled from its appearance uncertainty (e.g., in its color, \mathbf{f}_i). While this is a strong simplification, it is a common and effective strategy that allows us to efficiently estimate the parameter-wise variances.

We update these diagonal FIM entries, denoted $\mathcal{I}_{t,i}$, continuously using an exponential moving average (EMA) of the squared gradients [KB17]:

$$\mathcal{I}_{t,i} = \alpha_t \mathcal{I}_{t-1,i} + (1 - \alpha_t) [\nabla_{\theta_i} \ell_t]^2 \quad (8)$$

The EMA schedule, controlled by a linearly decaying α_t , where $\alpha_t = 0.95 \times (1 - t/T)$, smooths noisy gradients early in training. Substituting this tractable diagonal approximation into our object-aware uncertainty propagation (Eq. 7) yields our final formulation:

$$\Sigma_{C,k}(u) = (M_k(u))^2 J_u (\text{diag } \mathcal{I}_t + \lambda \mathbf{I})^{-1} J_u^\top \quad (9)$$

By summing the trace of $\Sigma_{C,k}(u)$ over all pixels corresponding to object k , we obtain a scalar score that guides our active view selection.

4. Experiments

4.1. Experimental Setup

Dataset We conduct our evaluation across three public datasets for a comprehensive experiment. **Mip-NeRF 360** [BMV*22] contains four bounded indoor rooms with strong specular clutter and five unbounded outdoor scenes with foliage occlusion and high dynamic range lighting. We follow the 3DGS protocol [KKLD23]: every 8th view is held out for testing. We also experiment on **Light-Field (LF)** dataset [YSHWSH16], which offers four tabletop objects *torch*, *statue*, *basket*, and *africa* captured by a motorised gantry. A salient trait is the *foreground-centric framing*: each target object remains centred across all views, yielding stable masks from SAM-2 and making the dataset ideal for evaluating *per-object* calibration. In addition we target the *train* and *truck* from **Tanks & Temples (TNT)** [KPZK17], which offers large-scale, drone-style outdoor captures characterised by long-baseline parallax and strong depth discontinuities. Inspired by the sparse-view protocol

Table 1: **Active View Selection** on Mip-NeRF360, Tanks&Temples, and LF datasets. "Panoramic" evaluates the full image; "Object-aware" evaluates only inside the object mask. Rows denote selection policies.

Method	Metrics	Mip-NeRF360			LF			Tanks & Temples		
		PSNR \uparrow	SSIM \uparrow	LPIPS \downarrow	PSNR \uparrow	SSIM \uparrow	LPIPS \downarrow	PSNR \uparrow	SSIM \uparrow	LPIPS \downarrow
Random		17.9140	0.5640	0.4300	19.0857	0.6646	0.2669	15.8784	0.5365	0.3720
ActiveNeRF		17.8890	0.5330	0.4140	21.2263	0.7691	0.1742	16.2918	0.5892	0.2514
BayesRays		18.8120	0.5730	0.4210	21.9232	0.7628	0.1752	16.9322	0.6091	0.3252
FisherRF		20.3510	0.6010	0.3610	23.6450	0.8323	0.1651	17.3684	0.6296	0.3091
GauSS-MI		20.8150	0.6433	0.2710	23.9820	0.8354	0.1628	17.4210	0.6315	0.2425
OUGS		20.6099	0.6453	0.2727	23.7014	0.8058	0.1726	17.2666	0.6125	0.2468

Object-Aware										
Random		26.3382	0.9732	0.0266	31.0709	0.9866	0.0227	24.6778	0.9306	0.1349
FisherRF		26.4312	0.9731	0.0276	30.82740	0.9813	0.0231	23.4830	0.9208	0.1396
GauSS-MI		27.3012	0.9764	0.0258	30.9742	0.9830	0.0226	24.9832	0.9318	0.1336
OUGS		29.6099	0.9813	0.0241	32.1856	0.9888	0.0221	26.2533	0.9333	0.1169

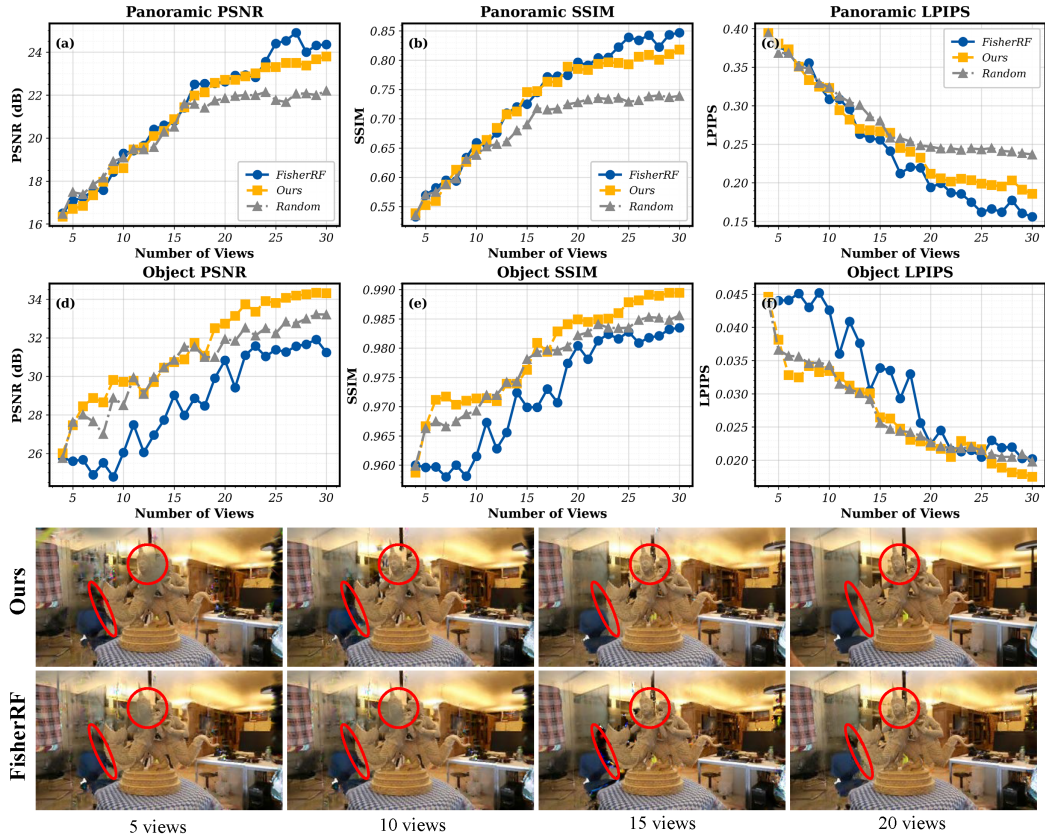


Figure 4: **Object-aware approach speeds up convergence.** Curves are recorded on the *statue* scene of the LF dataset as new views are added. Top row: panoramic PSNR/SSIM/LPIPS; middle row: the same metrics evaluated only inside the object mask. Bottom strip: visual progression at 5, 10, 15 and 20 views (ours in the first row, FisherRF below); red circles mark regions where the competing method keeps struggling while our reconstruction sharpens steadily.

of Shen [SAMNR22], we additionally include intentionally biased and imbalanced camera orbits. They exacerbate parallax/occlusion artifacts and thus form a stress test for Fisher-based uncertainty modeling. All RGB frames are kept at full original resolution to preserve fine geometric cues; no cropping or scaling is applied.

Baselines We compare our approach against several state-of-the-art methods that explicitly model uncertainty for *next-best-view* (NBV) selection. Our baseline pool includes: *ActiveNeRF* [PLSH22], *FisherRF* [JLD24], and *Bayes' Rays* [GRS*24]. Furthermore, to ensure a thorough comparison against the state-



Figure 5: **Qualitative result on Mip-NeRF360.** From left to right are ground truth, Ours (OUGS), FisherRF, and Random. Each row corresponds to a different scene. 20 views were selected to train a model and render the result on the test set. The blue box circles the object of interest, while the red box circles some of the background.

of-the-art, we include *GauSS-MI* [XCZ*25], a recent information-theoretic method that represents the state-of-the-art in scene-level active reconstruction. We also note the concurrent work *POPGS* [WAM*25], which also focuses on next best view selection. However, as its implementation was not publicly available during our experimental phase, a direct quantitative comparison was not feasible. All baselines are trained with their publicly released repositories using the authors’ default hyper-parameters, learning-rate schedules, and random seeds. To further control for segmentation bias, we feed the identical For fairness, the same SAM-2 probability masks are used for all baselines wherever applicable; if a method does not support masked view scoring, masks are used only for object-only evaluation while keeping its original selection policy. NBV selection is executed with the settings recommended

in the respective papers, ensuring a fair, apples-to-apples comparison. **Metrics** Our object-aware uncertainty estimation algorithm was evaluated based on render quality for the object and scene. Hence, we apply PSNR, SSIM, and LPIPS to evaluate the result. We report each metric on the average result of each scene of a specific dataset, and list a comparison result under the same configuration. Following the experimental protocol of [GRS*24], we quantify the quality of our predictive uncertainty using the Area Under the Sparsification Error curve (AUSE), a widely-adopted metric in depth-estimation literature. For every test image we first compute the per-pixel absolute error and the corresponding predicted uncertainty. We then iteratively mask out the top $t\%$ of pixels ($t = 1, \dots, 100$) in descending order of predicted uncertainty (highest-uncertainty first). At each sparsification level, we compute

Table 2: **Validation of our parameter-centric FIM as a standalone uncertainty estimator.** To isolate the quality of our core uncertainty model, we evaluate it on the full scene without any object-aware masks. The table reports the Area Under the Sparsification Error (AUSE), a rigorous metric for uncertainty quality (lower is better). Our method demonstrates highly competitive or superior performance against prior art across all scenes, confirming that our physically-grounded FIM formulation is a robust and accurate uncertainty estimator in its own right.

	africa		basket		statue		torch		TNT-Train		TNT-Truck	
	$\Delta\text{MSE}\downarrow$	$\Delta\text{MAE}\downarrow$	$\Delta\text{MSE}\downarrow$	$\Delta\text{MAE}\downarrow$	$\Delta\text{MSE}\downarrow$	$\Delta\text{MAE}\downarrow$	$\Delta\text{MSE}\downarrow$	$\Delta\text{MAE}\downarrow$	$\text{MSE}\downarrow$	$\text{MAE}\downarrow$	$\text{MSE}\downarrow$	$\text{MAE}\downarrow$
ActiveNeRF	1.123	0.958	0.642	0.546	0.818	0.732	1.513	1.246	1.279	1.076	0.994	0.438
Bayes' Rays	0.445	0.271	0.326	0.284	0.192	0.182	0.342	0.224	0.822	0.689	0.865	0.529
FisherRF	0.181	0.186	0.212	0.225	0.191	0.178	0.247	0.254	0.892	0.632	0.843	0.589
OUGS	0.192	0.187	0.122	0.131	0.181	0.181	0.248	0.217	0.787	0.589	0.651	0.487

the mean residual error of the retained pixels under both MAE and MSE and trace two corresponding sparsification-error curves; integrating each curve yields AUSE_{MAE} and AUSE_{MSE} , whose mutual consistency offers a more rigorous and reliable assessment of our uncertainty estimates.

Implementation Details.

Following SoTA next-best-view (NBV) [WAM*25] optimisation and uncertainty estimation, we evaluate on the benchmark datasets in Sec. 4.1. The 3D Gaussians are initialised with COLMAP [SF16], and object masks are obtained from SAM2 [RGH*24] to isolate the target object. NBV planning follows FisherRF [JLD24]: four initial views are selected using the farthest-point strategy, followed by 100 epochs of training and the addition of a new view chosen by the highest predicted uncertainty within the object mask. This process repeats until 20 views are reached, after which the model is optimised for 30k iterations with the default 3D Gaussian Splatting [KKLD23] schedule.

4.2. Quantitative Results

Our primary quantitative evaluation, presented in Table 1, reveals a clear and compelling story about the state of active 3D reconstruction. We analyze the results at two levels of granularity: the full scene and the object of interest.

Scene-Level Panoramic Performance. In the panoramic evaluation, which assesses the entire rendered view, the information-theoretic method **GauSS-MI establishes itself as the new state-of-the-art**, achieving the best results across most metrics and datasets. This highlights the effectiveness of maximizing information gain for comprehensively capturing complex scenes. Our method, OUGS, remains highly competitive in this setting. Notably, OUGS's performance is on par with or second only to GauSS-MI, and it consistently outperforms the previous FIM-based method, FisherRF. This confirms that our parameter-centric uncertainty formulation is a robust and effective replacement for pixel-level gradient approximations, even for global reconstruction tasks.

Object-Aware Performance. The core strength and primary contribution of our approach are revealed when the evaluation is restricted to the object of interest (*Object-Aware* rows). In this critical, object-centric setting, the performance hierarchy shifts dramatically. **OUGS consistently and substantially outperforms all other methods, including the panoramic SOTA GauSS-MI,**

across every dataset. This significant performance gap validates our central hypothesis and directly addresses the limitations of scene-level methods. While approaches like GauSS-MI and FisherRF are powerful, their view selection process is inevitably diluted by background clutter. By explicitly disentangling object uncertainty from the environment, our method allocates the finite view budget far more effectively, leading to a dramatic and consistent improvement in reconstruction fidelity for the target object.

Convergence and Visual Analysis. Figure 4 illustrates the convergence behavior, comparing our approach against the FIM-based FisherRF. While both methods track closely in the panoramic evaluation (top row), the object-only plots (middle row) show the stark advantage of our strategy. OUGS achieves sharp gains in PSNR and SSIM early in the process by immediately prioritizing object-centric views, whereas FisherRF's progress on the object is slower due to distractions from background gradients. These quantitative differences are also visually evident in the rendered results (bottom row). As more views are added, OUGS rapidly sharpens object details, while FisherRF continues to struggle with the same regions, sometimes even prioritizing background elements at the expense of the object of interest.

4.3. Qualitative Results

Figure 5 provides a qualitative comparison on the Mip-NeRF 360 dataset. To specifically analyze the behavior of uncertainty estimation based on the Fisher Information Matrix, we focus the visual comparison on our method, FisherRF, and a random baseline.

The results clearly illustrate the impact of our object-aware strategy. Across all scenes, our reconstructions remain visually closest to the ground truth in the regions of interest (blue boxes). On the *stump* scene, for example, the slender bark fibres are sharply delineated in our result, whereas they are rendered as blurred or are entirely missing by FisherRF. This reveals the fundamental difference in FIM-based approaches: FisherRF, however, often produces a cleaner background (red boxes). This stems from its scene-level Fisher information score; high-gradient background textures can dominate the score and steer the next-best-view search away from the object. Our method, by design, resists this distraction. Random sampling, while uninformed, spreads views uniformly and therefore sometimes captures object-centric angles, leading to occasional details that surpass FisherRF, but this comes at the cost of high variance and no guarantees. The visual evidence strongly

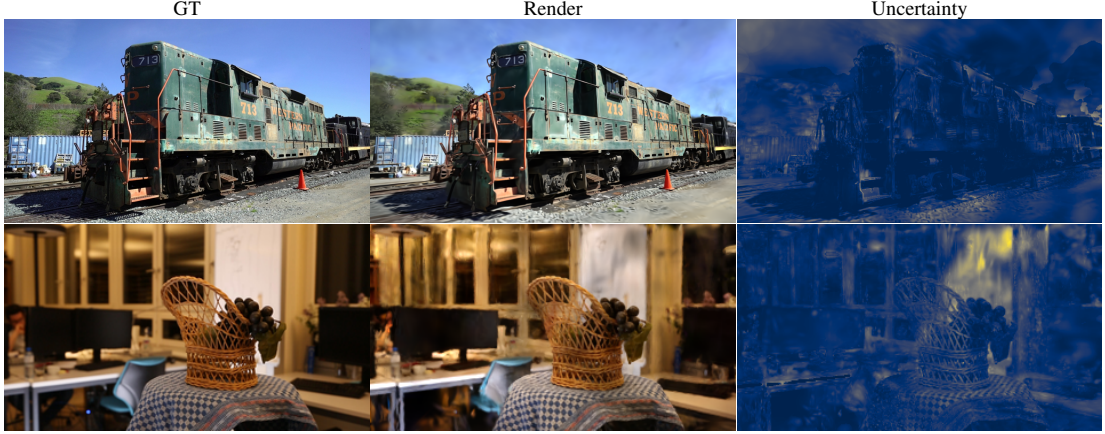


Figure 6: **Qualitative validation of our parameter-centric uncertainty.** These results on the TNT-Train (top) and LF-Basket (bottom) scenes showcase the remarkable accuracy of our uncertainty estimation. The uncertainty heatmap (right column, yellow indicates high uncertainty) precisely localizes the regions where the final rendering (middle column) deviates from the ground truth (left column), such as blurry structures and ghosting artifacts. This strong visual correlation demonstrates the effectiveness of our physically-grounded model in predicting and explaining rendering errors.

indicates that our method preserves object detail most faithfully. The modest artifacts that may appear at the image periphery do not outweigh the substantial and consistent gains in the target region, confirming the effectiveness of our object-aware formulation.

4.4. Ablation Study

Evaluating the FIM-based Uncertainty Estimation

We assess the effectiveness of our FIM-based uncertainty approximation in Section 3.3. To enable a fair comparison with alternative methods, we compute the sparsification error (AUSE) over the entire scene, without using the object-centric probability mask—after training 3DGS on the full dataset. AUSE measures the quality of uncertainty calibration. Specifically, it quantifies how the prediction error decreases as the most uncertain pixels are progressively removed. A well-calibrated uncertainty estimate will prioritize removing high-error pixels first, leading to a steep drop in error. The area under this curve captures the cumulative deviation from ideal sparsification; lower AUSE indicates better uncertainty estimates, meaning the uncertainty scores are more aligned with actual prediction errors.

Table 2 shows the results on two scenes from the TNT dataset and all scenes from the LF dataset. Our method achieves the lowest AUSE scores on both TNT scenes, outperforming FisherRF [JLD24], ActiveNeRF [PLSH22], and Bayes’Rays [GRS*24]. On the LF dataset, our approach also yields competitive results across all scenes. Figure 6 complements these findings with a visual comparison: uncertainty highlighted by our model (yellow overlay) concentrates on background regions that later exhibit blur or ghosting artifacts, while high-confidence areas remain artifact-free. These results indicate that our parameter-level uncertainty estimation not only improves overall reconstruction fidelity but also more precisely localizes residual errors.

Assessing the Role of Probability Mask Quality

To investigate how the quality of the soft mask influences our object-aware uncertainty estimation, we simulate mask degradation by varying the threshold value from 0.1 to 0.9 and plot the corresponding object level AUSE scores. Pixels with probabilities above the threshold are considered part of the object. At low threshold values (left side of the plot), the mask includes more unwanted background regions, leading to suboptimal view selection and higher (worse) AUSE scores. As the threshold increases, the mask becomes more focused on the object, improving performance and reaching an optimal AUSE around 0.5—where the mask best isolates the object while excluding background clutter. Beyond this point, further increases in the threshold aggressively remove less salient object regions, slightly degrading performance as informative areas are excluded.

Analysis of the EMA Update Schedule

Our FIM approximation relies on an online update of the diagonal entries using an EMA of squared gradients. A key design choice is our decaying momentum schedule for the EMA parameter, $\alpha_t = 0.95 \times (1 - t/T)$, which prioritizes stability early in training (high momentum) and faster adaptation later on (low momentum). To validate this choice, we conduct an ablation study comparing our proposed schedule against simpler alternatives with a constant momentum. We evaluate the final object-aware PSNR on the LF-Statue scene after 20 actively selected views.

The results, presented in Table 3, confirm the effectiveness of our proposed strategy. A constant high momentum ($\alpha_t = 0.99$) is overly cautious, smoothing too much and preventing the model from adapting quickly enough, resulting in lower PSNR. Conversely, a constant low momentum ($\alpha_t = 0.9$) is too reactive to noisy gradients, leading to an unstable FIM estimate and the worst performance. Our decaying schedule strikes the optimal balance,

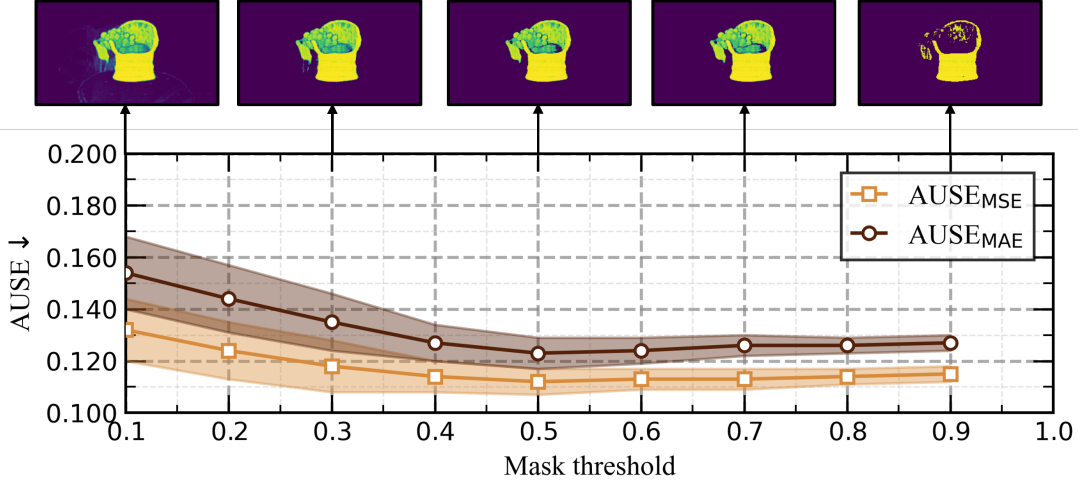


Figure 7: **Analysis of semantic mask quality on object-aware uncertainty.** We investigate the sensitivity of our method to the quality of the probability mask by varying its binarization threshold. The plot of object-level AUSE (lower is better) reveals a clear optimal range. At low thresholds, the mask is too permissive and includes distracting background regions, which inflates the uncertainty error. Conversely, at very high thresholds, the mask becomes overly aggressive and erodes parts of the object, discarding valuable information and again degrading performance.

Table 3: Ablation on the EMA update schedule, evaluated on the LF-Statue scene. Our decaying momentum strategy outperforms all constant momentum alternatives.

EMA Schedule Strategy	Object-Aware PSNR (dB) \uparrow
No EMA (Instantaneous)	29.52
Low Momentum ($\alpha_t = 0.90$)	31.63
Medium Momentum ($\alpha_t = 0.95$)	31.91
High Momentum ($\alpha_t = 0.99$)	32.04
Ours (Decaying Momentum)	32.18

achieving the highest PSNR. This validates that our carefully designed "slow-start, fast-finish" update strategy is crucial for robustly estimating the FIM online and contributes significantly to the final reconstruction quality.

5. Limitations and Future Work

While our framework demonstrates a significant advancement in object-centric active reconstruction, we acknowledge several limitations that open up exciting avenues for future research. Our focus is object-centric NBV; scene-level SOTA methods remain complementary when global coverage is prioritized. Besides, our method’s effectiveness is contingent upon the availability and quality of a semantic mask for the object of interest. Future work could explore methods for weakly-supervised object discovery to create a more self-contained system. The current formulation is also designed to optimize for a single object; extending it to handle multiple targets simultaneously, perhaps via a dynamic weighting of their respective uncertainties, presents an interesting challenge. Furthermore, for computational tractability, our method approximates the

full Fisher Information Matrix with its diagonal entries. This assumes independence between the different physical parameters of a Gaussian, which is a strong simplification. Future work could investigate more structured approximations of the FIM, such as a block-diagonal matrix for each Gaussian, to capture parameter correlations as a trade-off between computational cost and theoretical fidelity. Finally, scaling the online FIM updates for extremely large-scale scenes remains a challenge, suggesting a need for more efficient update or pruning strategies.

6. Conclusion

We introduced OUGS, an object-aware uncertainty estimation framework for active view selection in 3DGS. Our work presents a fundamental shift in how uncertainty is modeled for explicit representations. By deriving uncertainty directly from the physical parameters of the 3D Gaussian primitives, we establish a more principled and interpretable link between the 3D scene representation and the rendered 2D image. Our method projects this parameter-level covariance into pixel space and, by coupling it with semantic masks, produces an uncertainty score that effectively disentangles the object of interest from its environment. This is enabled by an efficient diagonal FIM update scheme that makes the approach computationally tractable. When integrated into a next-best-view loop, our method consistently and substantially outperforms state-of-the-art baselines in the critical task of object-centric reconstruction, achieving sharper results under the same view budget. Notably, our underlying uncertainty model also proves to be highly competitive for global scene reconstruction. Ultimately, these results underscore the importance of disentangling object-level uncertainty from background clutter for efficient, high-fidelity active

References

- [BKA*16] BIRCHER A., KAMEL M., ALEXIS K., OLEYNIKOVA H., SIEGWART R.: Receding horizon "next-best-view" planner for 3d exploration. In *2016 IEEE International Conference on Robotics and Automation (ICRA)* (2016), pp. 1462–1468. doi:10.1109/ICRA.2016.7487281. 3
- [BMV*22] BARRON J. T., MILDENHALL B., VERBIN D., SRINIVASAN P. P., HEDMAN P.: Mip-nerf 360: Unbounded anti-aliased neural radiance fields, 2022. URL: <https://arxiv.org/abs/2111.12077>, arXiv:2111.12077. 4
- [Bon08] BONGARD J.: Probabilistic robotics. sebastian thrun, wolfram burgard, and dieter fox. (2005, mit press.) 647 pages. *Artificial Life* 14, 2 (2008), 227–229. doi:10.1162/artl.2008.14.2.227. 4
- [CKD*25] CELAREK A., KOPANAS G., DRETTAKIS G., WIMMER M., KERBL B.: Does 3d gaussian splatting need accurate volumetric rendering?, 2025. URL: <https://arxiv.org/abs/2502.19318>, arXiv:2502.19318. 1
- [CLK11] CHEN S., LI Y., KWOK N. M.: Active vision in robotic systems: A survey of recent developments. *The International Journal of Robotics Research* 30, 11 (2011), 1343–1377. 1, 3
- [GRS*24] GOLI L., READING C., SELLÁN S., JACOBSON A., TAGLIASACCHI A.: Bayes' Rays: Uncertainty quantification in neural radiance fields. *CVPR* (2024). 1, 5, 6, 8
- [HD25] HAN C., DUMERY C.: View-dependent uncertainty estimation of 3d gaussian splatting, 2025. URL: <https://arxiv.org/abs/2504.07370>, arXiv:2504.07370. 1, 2
- [JLD24] JIANG W., LEI B., DANILIDIS K.: Fisherrf: Active view selection and uncertainty quantification for radiance fields using fisher information, 2024. URL: <https://arxiv.org/abs/2311.17874>, arXiv:2311.17874. 1, 3, 5, 7, 8
- [KB17] KINGMA D. P., BA J.: Adam: A method for stochastic optimization, 2017. URL: <https://arxiv.org/abs/1412.6980>, arXiv:1412.6980. 4
- [KKLD23] KERBL B., KOPANAS G., LEIMKÜHLER T., DRETTAKIS G.: 3d gaussian splatting for real-time radiance field rendering, 2023. URL: <https://arxiv.org/abs/2308.04079>, arXiv:2308.04079. 1, 3, 4, 7
- [KMKS24] KLASSON M., MEREU R., KANNALA J., SOLIN A.: Sources of uncertainty in 3d scene reconstruction, 2024. URL: <https://arxiv.org/abs/2409.06407>, arXiv:2409.06407. 1
- [KPZK17] KNAPITSCH A., PARK J., ZHOU Q.-Y., KOLTUN V.: Tanks and temples: benchmarking large-scale scene reconstruction. *ACM Trans. Graph.* 36, 4 (July 2017). URL: <https://doi.org/10.1145/3072959.3073599>, doi:10.1145/3072959.3073599. 4
- [KSH22] KIM M., SEO S., HAN B.: Infonerf: Ray entropy minimization for few-shot neural volume rendering, 2022. URL: <https://arxiv.org/abs/2112.15399>, arXiv:2112.15399. 3
- [LC24] LI R., CHEUNG Y.-M.: Variational multi-scale representation for estimating uncertainty in 3d gaussian splatting. In *Advances in Neural Information Processing Systems* (2024), Globerson A., Mackey L., Belgrave D., Fan A., Paquet U., Tomczak J., Zhang C., (Eds.), vol. 37, Curran Associates, Inc., pp. 87934–87958. URL: https://proceedings.neurips.cc/paper_files/paper/2024/file/a076d0d1ed77364fc57693bdee1958fb-Paper-Conference.pdf. 2
- [LMV*17] LY A., MARSMAN M., VERHAGEN J., GRASMAN R., WAGENMAKERS E.-J.: A tutorial on fisher information, 2017. arXiv:1705.01064. 4
- [MST*20] MILDENHALL B., SRINIVASAN P. P., TANCİK M., BARRON J. T., RAMAMOORTHY R., NG R.: Nerf: Representing scenes as neural radiance fields for view synthesis. In *CVPR* (2020), pp. 612–621. 1
- [NBM*21] NIEMEYER M., BARRON J. T., MILDENHALL B., SAJJADI M. S. M., GEIGER A., RADWAN N.: Regnerf: Regularizing neural radiance fields for view synthesis from sparse inputs, 2021. URL: <https://arxiv.org/abs/2112.00724>, arXiv:2112.00724. 1
- [PLSH22] PAN X., LAI Z., SONG S., HUANG G.: Activenerf: Learning where to see with uncertainty estimation, 2022. URL: <https://arxiv.org/abs/2209.08546>, arXiv:2209.08546. 3, 5, 8
- [RGH*24] RAVI N., GABEUR V., HU Y.-T., HU R., RYALI C., MA T., KHEDR H., RÄDLE R., ROLLAND C., GUSTAFSON L., MINTUN E., PAN J., ALWALA K. V., CARION N., WU C.-Y., GIRSHICK R., DOLLÁR P., FEICHTENHOFER C.: Sam 2: Segment anything in images and videos, 2024. URL: <https://arxiv.org/abs/2408.00714>, arXiv:2408.00714. 7
- [RZH*23] RAN Y., ZENG J., HE S., CHEN J., LI L., CHEN Y., LEE G., YE Q.: Neurar: Neural uncertainty for autonomous 3d reconstruction with implicit neural representations. *IEEE Robotics and Automation Letters* 8, 2 (Feb. 2023), 1125–1132. URL: <http://dx.doi.org/10.1109/LRA.2023.3235686>, doi:10.1109/LRA.2023.3235686. 3
- [SAMNR22] SHEN J., AGUDO A., MORENO-NOGUER F., RUIZ A.: Conditional-flow nerf: Accurate 3d modelling with reliable uncertainty quantification, 2022. URL: <https://arxiv.org/abs/2203.10192>, arXiv:2203.10192. 5
- [SF16] SCHONBERGER J. L., FRAHM J.-M.: Structure-from-motion revisited. In *Proceedings of the IEEE Conference on Computer Vision and Pattern Recognition (CVPR)* (June 2016). 7
- [SVM24] SAVANT L., VALSESIA D., MAGLI E.: Modeling uncertainty for gaussian splatting, 2024. URL: <https://arxiv.org/abs/2403.18476>, arXiv:2403.18476. 2
- [TCZ*25] TAN Z., CHEN X., ZHANG J., FENG L., HU D.: Uncertainty-aware normal-guided gaussian splatting for surface reconstruction from sparse image sequences, 2025. URL: <https://arxiv.org/abs/2503.11172>, arXiv:2503.11172. 2
- [WAM*25] WILSON J., ALMEIDA M., MAHAJAN S., LABRIE M., GHAFARI M., GHASEMALIZADEH O., SUN M., KUO C.-H., SEN A.: Pop-gs: Next best view in 3d-gaussian splatting with p-optimality, 2025. URL: <https://arxiv.org/abs/2503.07819>, arXiv:2503.07819. 3, 6, 7
- [XCZ*25] XIE Y., CAI Y., ZHANG Y., YANG L., PAN J.: Gaussmi: Gaussian splatting shannon mutual information for active 3d reconstruction, 2025. URL: <https://arxiv.org/abs/2504.21067>, arXiv:2504.21067. 2, 3, 6
- [XDM*24] XUE S., DILL J., MATHUR P., DELLAERT F., TSOTRAS P., XU D.: Neural visibility field for uncertainty-driven active mapping, 2024. URL: <https://arxiv.org/abs/2406.06948>, arXiv:2406.06948. 3
- [YSHWSH16] YÜCER K., SORKINE-HORNUNG A., WANG O., SORKINE-HORNUNG O.: Efficient 3d object segmentation from densely sampled light fields with applications to 3d reconstruction. *ACM Trans. Graph.* 35, 3 (Mar. 2016). URL: <https://doi.org/10.1145/2876504>, doi:10.1145/2876504. 4

Appendix A: Jacobian–Covariance Propagation

To propagate parameter uncertainty into pixel space we expand the rendered colour $C(u; \theta)$ around its MAP estimate θ^* using a second-order Taylor series:

$$\mathbb{E}[C(u; \theta)] \approx C(u; \theta^*) + \nabla_{\theta} C(u; \theta^*)^{\top} (\theta - \theta^*) + \frac{1}{2} (\theta - \theta^*)^{\top} H_u (\theta - \theta^*), \quad (10)$$

where $H_u \in \mathbb{R}^{d \times d}$ is the Hessian of C at θ^* and $\delta\theta \triangleq \theta - \theta^*$. The linear term is *empirically two orders of magnitude smaller* than the quadratic term under i.i.d. zero-mean residuals; we therefore neglect it in what follows.

Keeping only the leading non-zero term in the second central moment yields the classic *Jacobian–Covariance law*:

$$\text{Var}[C(u; \theta)] \approx J_u \Sigma J_u^{\top}, \quad J_u := \left. \frac{\partial C(u; \theta)}{\partial \theta} \right|_{\theta^*} \in \mathbb{R}^{3 \times d}. \quad (11)$$

Here J_u measures how each parameter perturbs the RGB value at pixel u . Its element $[J_u]_{kl} = \partial C_k(u; \theta^*) / \partial \theta_l$ quantifies the influence of the l -th parameter on the k -th channel.

The truncation error of (11) obeys

$$\mathcal{E} \leq \frac{1}{4} \|H_u\|_F \|\Sigma\|_F^2 + \mathcal{O}(\|\Sigma\|_F^3), \quad (12)$$

which vanishes as the Gaussian parameters become well-constrained ($\|\Sigma\|_F \rightarrow 0$) since $\|\Sigma\|_F \ll \|H_u^{-1}\|_F^{1/2}$.

Appendix B: FIM Approximation and Online Update

Full Fisher Matrix under Gaussian Image Noise

Assume each observed pixel is corrupted by independent Gaussian noise $\varepsilon(u) \sim \mathcal{N}(0, \sigma^2)$, so the ground-truth intensity satisfies $C_{\text{gt}}(u) = C(u; \theta) + \varepsilon(u)$. With the usual i.i.d. assumption, the negative log-likelihood—up to an irrelevant constant—is the per-pixel squared error

$$\ell_t = \frac{1}{2\sigma^2} \sum_u \|C_{\text{pred},t}(u; \theta) - C_{\text{gt},t}(u)\|_2^2,$$

(the sum runs over colour channels as well as pixels).

The Fisher information matrix (FIM) is defined as the noise expectation of the outer product of the log-likelihood gradients:

$$\mathcal{I} = \mathbb{E}_{\varepsilon} [\nabla_{\theta} \ell_t \nabla_{\theta} \ell_t^{\top}].$$

For a single pixel u , the gradient is

$$\begin{aligned} \nabla_{\theta} \ell_t(u) &= \frac{1}{\sigma^2} (C_{\text{pred},t}(u; \theta) - C_{\text{gt},t}(u)) \nabla_{\theta} C(u; \theta)^{\top} \\ &= -\frac{\varepsilon_t(u)}{\sigma^2} J_u^{\top}, \end{aligned}$$

where $J_u = \partial C(u; \theta) / \partial \theta$. Because the noise is independent across pixels, $\mathbb{E}[\varepsilon_t(u) \varepsilon_t(v)] = \sigma^2 \delta_{uv}$ with δ_{uv} the Kronecker delta, all cross-terms vanish, giving

$$\mathcal{I} = \frac{1}{\sigma^2} \sum_u J_u^{\top} J_u. \quad (13)$$

Stacking all per-pixel Jacobians row-wise gives $J = \begin{bmatrix} \vdots \\ J_u \\ \vdots \end{bmatrix} \in \mathbb{R}^{n_{\text{pix}} \times d}$, so the FIM can be written compactly as

$$\mathcal{I} = \frac{1}{\sigma^2} J^{\top} J, \quad (14)$$

where n_{pix} is the number of pixels in the batch and d the total parameter dimension. This dense $d \times d$ matrix captures all pairwise parameter interactions but is prohibitively large to store or invert.

Diagonal Approximation with Tikhonov Regularisation

The Laplace (Cramér–Rao) bound yields the posterior covariance $\Sigma \approx \sigma^2 (J^{\top} J + \lambda \mathbf{I}_d)^{-1}$. To avoid storing or inverting the dense matrix we keep only its diagonal:

$$\mathcal{I}^{\text{diag}} = \frac{1}{\sigma^2} \text{diag}(J^{\top} J), \quad \Sigma \approx (\mathcal{I}^{\text{diag}} + \lambda \mathbf{I}_d)^{-1}, \quad (15)$$

where $\mathcal{I}^{\text{diag}}$ is the diagonal Fisher approximation and $\lambda \sim 10^{-4}$ (fixed for all experiments) ensures numerical stability when $J^{\top} J$ is rank-deficient.

Exponential-Moving-Average (EMA) Update

During training we accumulate the diagonal Fisher entries online via an EMA of squared gradients:

$$\mathcal{I}_{t,i}^{(j)} = \alpha_t \mathcal{I}_{t-1,i}^{(j)} + (1 - \alpha_t) [\nabla_{\theta^{(j)}} \ell_t]^2, \quad \alpha_t = 0.95 (1 - t/T). \quad (16)$$

Here $\mathcal{I}_{t,i}^{(j)}$ approximates the (j, j) element of the diagonal Fisher $\mathcal{I}^{\text{diag}}$ for Gaussian i at iteration t , and T is the total number of optimisation steps. The schedule smoothly decays α_t from 0.95 to 0, providing heavy smoothing to noisy early gradients and faster adaptation toward the end. Equation (16) requires only one *AXPY* operation per parameter and no inter-device communication.

Object-Aware Pixel Covariance

With the diagonal Fisher approximation $\mathcal{I}_t^{\text{diag}} = \text{diag} \mathcal{I}_t$ we obtain the tractable object-aware covariance used in the main paper,

$$\Sigma_{C,k}(u) = (M_k(u))^2 J_u (\mathcal{I}_t^{\text{diag}} + \lambda \mathbf{I}_d)^{-1} J_u^{\top}, \quad (17)$$

where $M_k(u) \in [0, 1]$ is the soft mask for object k . Although $\mathcal{I}_t^{\text{diag}}$ is diagonal, the Jacobian J_u couples all parameters, so cross-channel interactions are preserved when propagating uncertainty to the image plane. Summing (17) over pixels with $M_k(u) > 0$ produces an uncertainty score for object k that drives next-best-view selection in a computationally tractable manner.